Journal of Geophysical Research – Planets

Supplementary Information for:

Wind-driven erosion and exposure potential at Mars 2020 Rover candidate landing sites

Matthew Chojnacki[*1], Maria Banks[2], and Anna Urso[1].

[1]Lunar and Planetary Laboratory, University of Arizona, Tucson, AZ, 85721-0063, USA (chojan1@pirl.lpl.arizona.edu), [2]NASA Goddard Space Flight Center, 8800 Greenbelt Road, Greenbelt, MD. *Corresponding Author

Contents of this file

Additional Supporting Information (Files uploaded separately)

Animations S1–S9

Introduction

Supplementary materials include a detailed methodology for the derivation of dune topography and change detection. Additionally, materials include two tables with detailed information for Mars 2020 candidate landing site regional sand flux (Table S1) and local change detection (Table S2) results. These tables are to supplement and complement with Tables 1-2. Three supplementary figures provide additional geographic context for candidate landing sites (Fig. S1, S3) and locations for local bedform change detection results (Fig. S1).

Included animations provide additional evidence for bedform activity or inactivity, while tables, figures, and text give further details. Animations S1, S4, and S6 were built using in-house software, which takes orthophoto subsets, stacks them in chronological order, and provides relevant context information such as Mars date (Mars year, L_s), the direction of north, and solar azimuth. As per convention, the solar longitude (L_s) range of 0°–360° defines a MY and 11 April 1955 (L_s =0°) is the start of the Mars calendar at MY01 (see Piqueux et al. (2015) for details). Other animations were generated from manually triangulated image subsets, often using an orthoimage as the base image (see Table S1), and constructed in Photoshop. Some of these latter manual animations do have some slight distortions (e.g., upper left of Animation S3) due to slight differences in image parameters (e.g., roll angle), but these do not affect interpretations of

unambiguous changes elsewhere. All animations were arranged with north as up and images are listed in Table S1. Compare with similar animated GIFs of migrating dunes at http://www.uahirise.org/sim/ and Chojnacki et al. (2017).

Section 1. Derivation of dune topography and change detection

To quantify dune heights and movement, high-resolution topography was derived using stereo photogrammetry via SOCET SET® BAE system software (see Kirk et al., 2008). The resulting DTMs possess a horizontal post spacing of 1 meter, where the quality of pixel matching is provided by SOCET SET as a RMS error that is typically 0.3–0.7 of the HiRISE pixel scale (i.e., 25 cm) (Kirk et al., 2008; Sutton et al., 2015) and are reported in those Planetary Data Systems products. These HiRISE Digital Terrain Models (DTMs) were registered to Mars Orbiter Laser Altimeter (MOLA) (Smith et al., 2001) shot points for absolute elevation. DTMs generally possess a vertical precision of ~30 cm based on the convergence angle and spatial resolution of the stereo pair (Kirk et al., 2003). Terrain artifacts created during the photogrammetric terrain generation due to bland or deeply shadowed areas were recognized and avoided in co-registered HiRISE Figure of Merit (FOM) maps (Mattson et al., 2012).

Stereo and monitoring images were then orthorectified to the DTM to allow change detection and bedform displacement quantification to be made. Bedform lee-front advancements were recorded in several locations per dune and then averaged, but obvious areas of avalanches were avoided. Most dunes measured were crecentric in morphology (e.g., barchan, barchanoid) so lee-front measurements were performed at the perceived center of the slip face. Using the product of the bedform migration rate (m/Earth-year) and height (m), bedform sediment fluxes ($m^3\ m^{-1}\ yr^{-1}$) were calculated (Ould Ahmedou et al., 2007; Bridges et al., 2012; Chojnacki et al., 2015).

For a few locations lacking stereo data and orthoimages, manual registration of map-projected sub-regions to common immobile tie points (e.g., craters, boulders) was used for change detection and measurements of bedform displacement, similar to prior work (Chojnacki et al., 2011; Bridges et al., 2011). To estimate dune heights for these locations, we employed a slip face length-height (H) technique (Bourke et al., 2006) and Eq. (1):

$$H = L_{SF} \times \tan\theta \quad (1)$$

where L_{SF} is the measured adjacent slip face length, and θ is the assumed angle of repose (33°; (Atwood-Stone & McEwen, 2013)). This approach provides a height underestimation as the dune crest is often stossward of the slip face, but dune heights obtain with this approach have been found to be typically within ~8% of those measured with DTMs (Chojnacki et al., 2017). Finally, change detection is optimal using images acquired at similar seasons (ΔL_s <20°) and viewing geometries (e.g., differences in phase angle of 12° or less). In some cases, less desirable image pairs with looser seasonal constraints were used for change detection and are noted in Table S1.

Section 2. Abrasion rates were estimates using sand fluxes

Abrasion rates were estimated using Eq. (2):

$$(S_a Q_i / z)(\alpha\cos\theta + \sin\theta), \quad (2)$$

where S_a is the abrasion susceptibility, Q_i is the interdune sand flux, z is the mean trajectory height on Mars, α is the ratio of saltation height to descending path length, and θ is the slope of the target material (ranged from 0° to 90°) (Bridges et al., 2012). A range of S_a values have been determined in the laboratory (Greeley et al., 1982) and a value of $2x10^{-6}$ was primarily used a for basaltic sediment targeting basaltic rock. A higher S_a value of $4.8x10^{-6}$ was also used to represent softer sedimentary rock (e.g., hydrocal or gypsum cement). Q_i can be estimated as roughly one-third of the average crest flux for the site (Ould Ahmedou et al., 2007). A range of 0.1 to 0.5 m was used for z (Kok, 2010), and ratios between 0.1 and 0.2 were used for α, similar to Bridges et al. (2012).

Table S1. HiRISE observations and sand transport results for Mars 2020 candidate landing site regional dune fields[a].

Landing Site and dune field location and ID[b]	Images	Time duration EY	Time duration MY	Method	Rate m/EY	Sediment flux $m^3\ m^{-1}\ EY^{-1}$
Holden / Eberswalde						
Roddy crater 3204-216	ESP_024913_1580 ESP_042860_1580	3.83	2.04	DTM	0.3 +/- 0.1	4.3 +/- 0.9
Holden 3263-257	ESP_034763_1540 ESP_043374_1540	1.84	0.98	DTM	0.3 +/-0.1	6.2 +/-1.1
SW Melas						
Ius Chasma 2766-071	PSP_003949_1725 ESP_039209_1725	7.52	4.0	Manual	0.3 +/-0.1	2.7 +/-0.7
C. Coprates Canyon* 2936-114	ESP_013587_1685 ESP_047318_1685	7.20	3.83	Manual	0.24 +/-0.1	3.8 +/-0.5
E. Ophir Chasma 2890-043	ESP_039525_1755 ESP_049019_1755	2.03	1.08	Manual	0.53 +/-0.1	4.6 +/-1.8
Hydrae Chasma* 2980-068	ESP_013033_1730 ESP_039209_1725	3.52	1.87	DTM	0.8 +/-0.4	5.0 +/-2.4
Mawrth						
E Becquerel crater 3518+215	PSP_001546_2015 ESP_037043_2015	7.57	4.03	DTM	0.2 +/-0.02	1.2 +/-0.5
W Becquerel crater 3515+212	ESP_016077_2015 ESP_042173_2015	5.57	2.96	DTM	0.2 +/-0.1	1.6 +/-0.8
NW Meridiani 3423+137	ESP_014429_1940 ESP_041224_1940	5.27	3.04	Manual	0.24 +/-0.1	3.1 +/-1.2
Oyama crater* 3396+232	ESP_034815_2035 ESP_042714_2035	1.68	0.90	DTM	0.68 +/-0.1	10.5 +/-2.7
McLaughlin crater 3374+216	PSP_009814_2020 ESP_036859_2020	5.71	3.03	DTM	0.8 +/-0.3	11.5 +/-2.5
Nili Fossae / Jezero / NE Syrtis						
Nili Fossae 0742+214	PSP_003086_2015 ESP_047049_2015	9.38	4.99	DTM	0.5 +/-0.2	7.2 +/-3.9
E Syrtis Major 0794+198	PSP_002110_2000 ESP_037475_2000	7.55	4.01	DTM	0.1 +/-0.03	8.4 +/-5.1
E. Toro in Isidis Planitia* 0730+171	ESP_014096_1975 ESP_044992_1975	6.59	3.51	DTM	0.29+/-0.8	9.6+/-4.7
Nili Patera 0672+086	PSP_005684_1890 ESP_023353_1890	3.8	2.0	DTM	0.77 +/-0.2	16.0 +/-4.5
Meroe crater* 0676+070	PSP_007754_1875 ESP_038280_1885	6.51	3.46	DTM	0.52 +/-0.2	16.9 +/-4.9

[a]Migration rates and sediment flux estimates are provided with mean and standard deviation values for the collective dune population at each monitoring location.
[b]Dune field site IDs, where the first four digits are the monitoring site's centroid east longitude, the last three digits are the site's latitude (each coordinate given to the first decimal place without the decimal), and the separating + or – sign indicating which hemisphere.
*Image pair temporal offsets from even increments of Mars years are noted with deviations of >0.10 Mars years.

Table S2. Local change detection[a] results for Mars 2020 candidate landing sites to be compared with Fig. S2.

Site	Images	Notes
Holden		
	PSP_002088_1530* ESP_028513_1530	Several areas along the eastern edge of the ellipse with TARs or megaripples were checked and no changes were detected.
	PSP_004211_1525 ESP_039471_1525	Areas southeast of the ellipse with TARs or megaripples were checked and no changes were detected.
Eberswalde		
	ESP_010553_1560* ESP_019757_1560*	Clear displacements of dark-toned bedform units (ripples) south of ellipse. No detection of megaripples and TARs within ellipse to the north.
	PSP_004000_1560 ESP_047185_1560	Displacements of dark-toned bedform unit (ripples) along delta toe and edge of ellipse. No detection of megaripples and TARs within ellipse (not mapped).
	PSP_010553_1560* ESP_048899_1560	No detection of megaripples and TARs within and northeast of ellipse.
SW Melas		
	PSP_007087_1700 ESP_044325_1700*	Small displacements (eastward) of small ripple patches north of the ellipse. No detection of TARs within ellipse, but minor ripple movement.
Mawrth		
	PSP_008469_2040* ESP_043426_2040	Several areas along the central ellipse with TARs or megaripples were checked and no changes were detected.
	PSP_004052_2045* ESP_050362_2045	Areas just northwest of the ellipse with megaripples were checked and no changes were detected.
Nili Fossae		
	PSP_003086_2015* ESP_047049_2015*	High flux sand dunes migrating (northwest) along with sand ripples ~2 km northwest of ellipse.
	PSP_006633_2010* ESP_046693_2015	Areas to the south of the ellipse near a small crater show subtle albedo changes, but not displacements of TARs. No movement detected for TARs on the east edge of the ellipse. Very small ripples.
	PSP_005354_2015 ESP_045915_2015	Migration of trough barchans and ripples (west-northwest) ~5 km southwest of the ellipses.

Jezero		
	PSP_007925_1990 ESP_037607_1990	Several sand dunes and ripples north of the ellipse within inlet valley were detected migrating west. Dunes have low fluxes (~1 $m^3 m^{-1} yr^{-1}$).
	PSP_002387_1985* ESP_037396_1985*	Area with small wind ripples on the eastern edge and within the ellipse were checked and small displacements were detected. Larger ripples or TARs were static (not mapped).
	PSP_002387_1985* ESP_037330_1990*	Area with small wind ripples north of and within the ellipse were checked and small displacements were detected. Larger ripples or TARs were static (not mapped).
NE Syrtis		
	ESP_026280_1975 ESP_034772_1980	Several sand dunes and ripples southwest of the ellipse were detected migrating west. Dunes have low fluxes (~1–4 $m^3 m^{-1} yr^{-1}$).
	ESP_017643_1980 ESP_043739_1975	Small displacements of wind ripples at base of cliff south of ellipse.
	ESP_015942_1980* ESP_050253_1980	Southwest area of the ellipse with TARs was checked and no changes were detected (not mapped). Small wind ripples occur at the base of mesas and possible changes were detected (not mapped).
	PSP_009217_1975 ESP_027625_1975*	Small displacements of wind ripples at base of cliff south of ellipse
Columbia Hills		
	PSP_001777_1650* ESP_046729_1650	Several areas within the Columbia Hills (El Dorado, El Cap) with large ripples were checked and no changes were detected. Ripples in craters within ellipse show no change.
	PSP_001777_1650* ESP_037709_1650	Several areas within the Columbia Hills (El Dorado, El Cap) with large ripples were checked and no changes were detected. Ripples in craters within ellipse show no change.
	PSP_006735_1650 ESP_043696_1655	Several craters with large ripples on the plains north of the Columbia Hills were checked and no changes were detected. Ripples in craters within ellipse show no change.
	ESP_035164_1655* ESP_044962_1655*	Several craters in overlapping orthos with large ripples were checked and no changes detected.
	PSP_009174_1655 ESP_044962_1655*	Several craters with large ripples and extracrater TARs were checked and no changes detected.

[a]Repeat HiRISE coverage of bedforms were investigated within and adjacent to the candidate ellipses (typically within a few ellipse diameters).
*Images were orthorectified, decreasing image distortions, and used as the base images for change detection.

Supplemental Figures

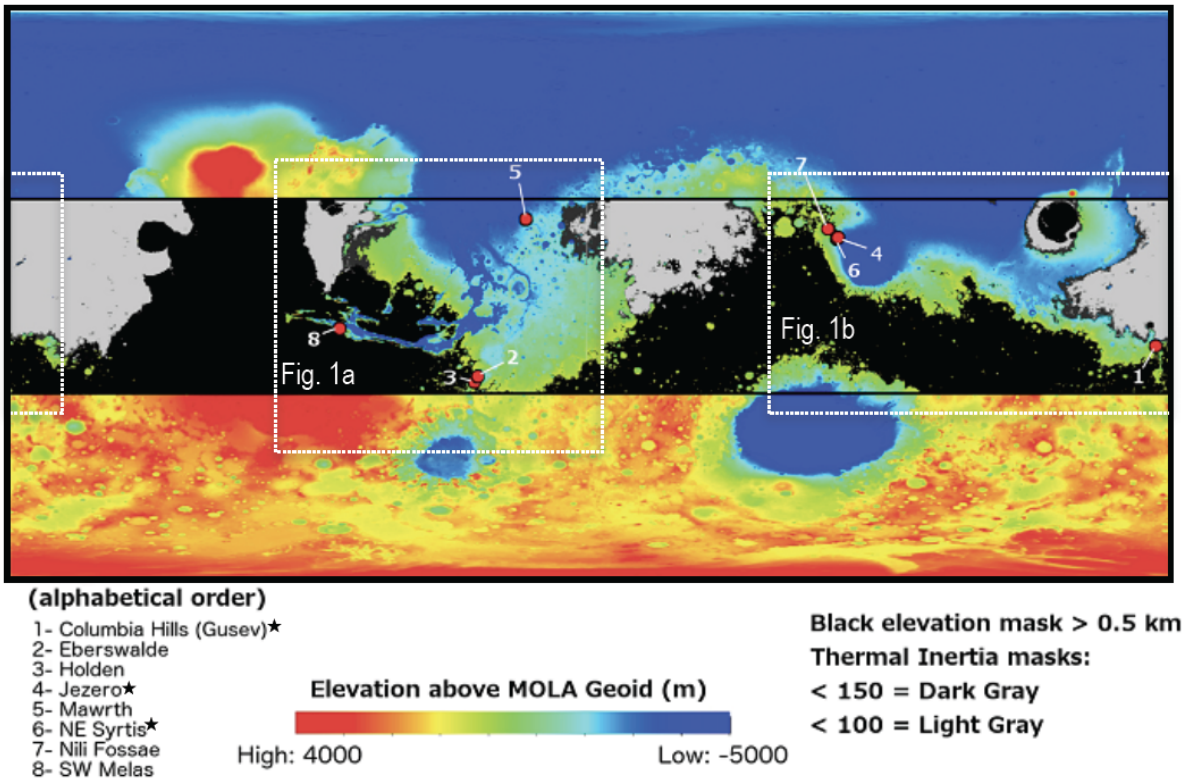

Figure S1. A map of Mars showing areas that meet the engineering constraints for landing the 2020 Mars rover that are within +/-30° latitude of the equator, below +0.5 km elevation, and that possess surfaces with thermal inertia >100–150 $Jm^{-2}K^{-1}s^{-1/2}$; surfaces outside of the elevation (black) and thermal inertia constraints (gray) are masked out. Background map is MOLA elevation where the required latitude range is indicated. Other restrictions were considered and include terrain relief, slopes, rock abundance, radar reflectivity, and surface load bearing capability. Locations of the candidate landing sites are also provided. Asterisks indicate the three down selected sites. See Golombek et al. (2015, 2016, 2017) and Golombek et al. (2012) for more details on their properties and geology. Modified from https://marsnext.jpl.nasa.gov/index.cfm.

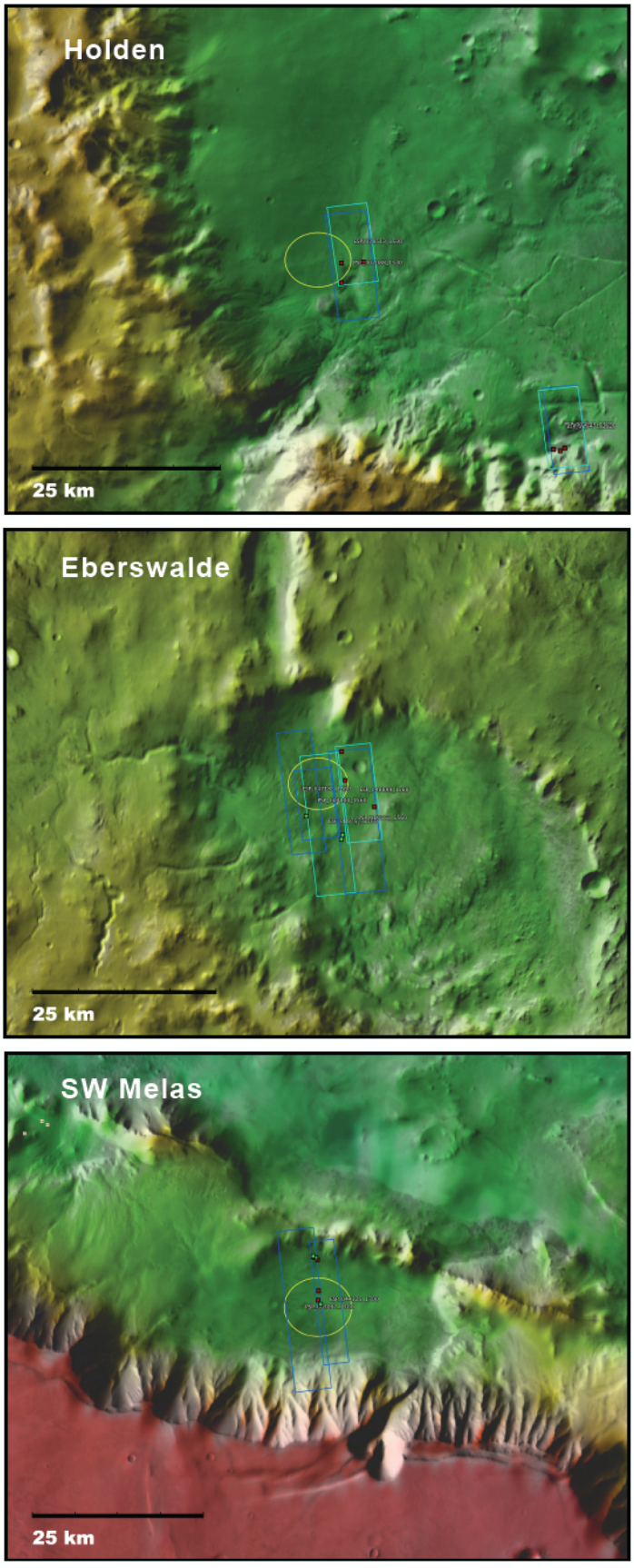

Figure S2.

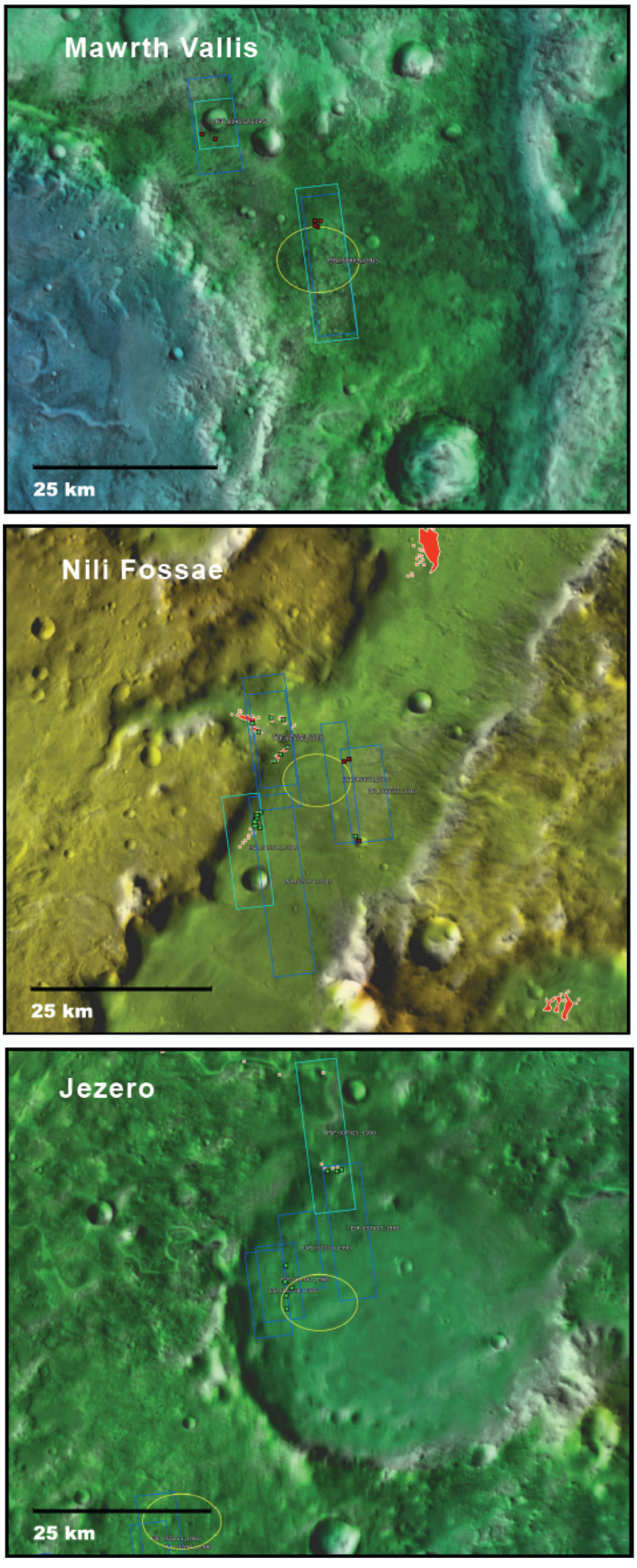

Figure S2. (continued)

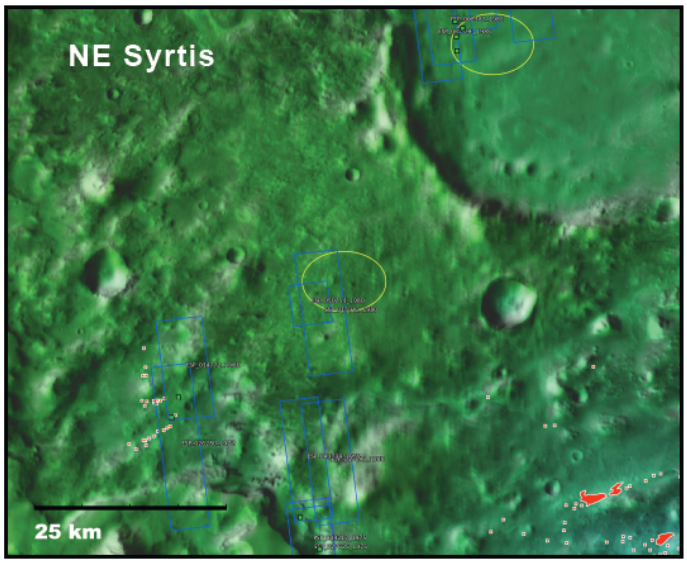

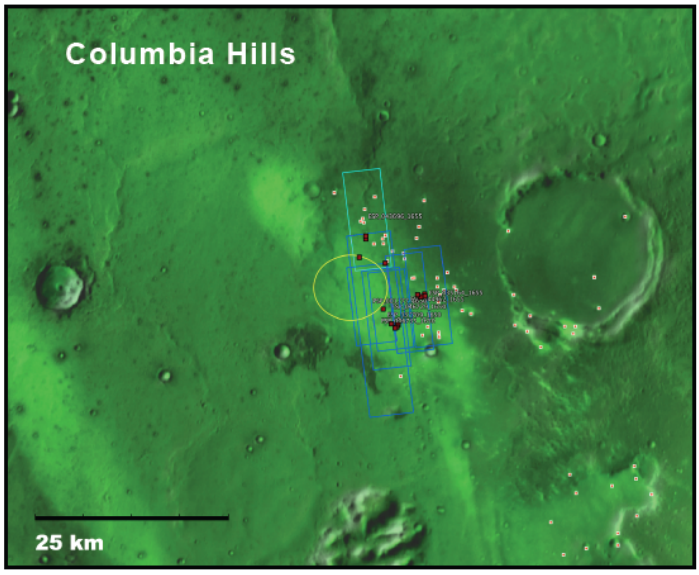

Figure S2. (continued) Subarea maps of candidate landing sites with results from local change detection analyses of bedforms located within or adjacent to landing ellipses (yellow). Bedform activity status provided with active dunes or ripples (green squares) and null detections of bedforms (auburn squares). Dune mapping results (or ripple fields for Columbia Hills) are also provided (red squares). Footprints and image IDs of HiRISE data used are shown. THEMIS Day-IR colorized with MOLA elevation. Compare with Table S1.

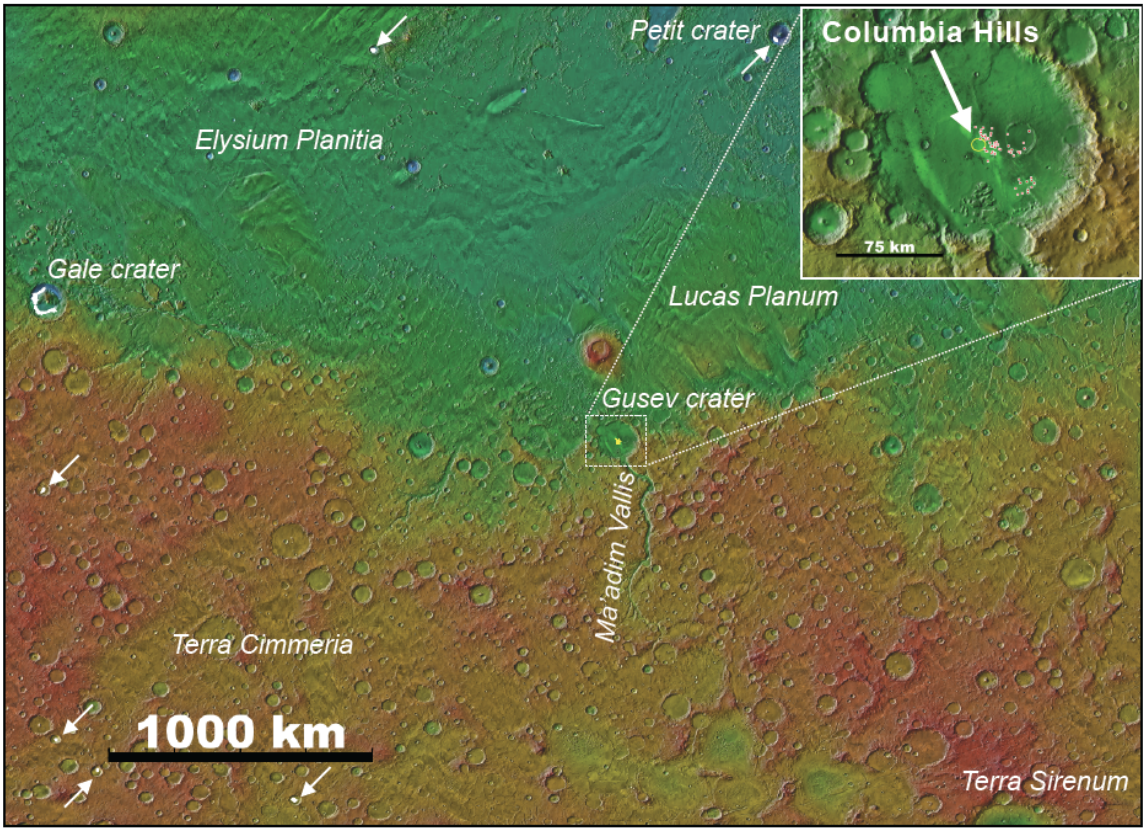

Figure S3. Subarea maps of Gusev crater/Columbia Hills and surrounding region. No dune fields were detected and mapped in the surrounding 1500 km by prior efforts (Hayward et al., 2014) or herein. Nearby dune fields such as Gale crater to the west, are active with low fluxes (Chojnacki et al., 2017). Prior global bedform monitoring efforts did not identify bedform locations in these regions, other than ones with static TARs (Bridges et al., 2011, 2013; Banks et al., 2015). (upper right) A closer view of Gusev crater area; same view as shown in Fig. 9a. THEMIS Day-IR colorized with MOLA elevation.

Animation Captions:

Animation S1. An animated time-step (orthorectified) sequence of wind ripples migrating southward across a (local) barchan dune north of the Holden candidate landing site ellipse. Slight dune lee-face advancement is also observable in the 1 Mars year between images (bottom right). Also see Fig. 2b.

Animation S2. An animated time-step sequence of dark (local) ripples migrating (white arrows) southward just south of the Eberswalde candidate landing site ellipse. Note the lack of movement in the underlying bright TARs to the right. Scene is ~220 m wide. Also see Fig. 2f.

Animation S3. An animated time-step sequence of dark (local) ripples migrating (white arrows) westward north of the SW Melas candidate landing site ellipse. Note the lack of movement in the underlying bright TARs. Scene is ~500 m wide. Note the slight distortions on the top left due to image geometry offsets. Also see Fig. 4d.

Animation S4. An animated time-step (orthorectified) sequence of high flux (regional) barchan dunes migrating south in McLaughlin crater over 4 Mars years. These intracrater dunes are to the west of the Mawrth candidate landing site ellipse. Also see similar occurrences shown in Fig. 5b.

Animation S5. An animated time-step sequence of large (local) ripples or TARs within the Mawrth candidate landing site ellipse. No ripple displacements were found. Scene is ~375 m wide. Also see similar occurrences shown in Fig. 5c-5d.

Animation S6. An animated time-step (orthorectified) sequence of high flux (local) barchan dunes just northeast of the Nili Fossae candidate landing site ellipse. These dunes likely migrated across the ellipse over the last few centuries. Also see Fig. 6d.

Animation S7. An animated time-step sequence of low albedo, inlet channel (local) dunes migrating west and just north of the Jezero candidate landing site ellipse. Note the dune lee-face displacement (white arrows) compared with the valley wall and static TARs. Scene is ~300 m wide. Also see Fig. 7c.

Animation S8. An animated time-step sequence of dark (local) ripples migrating (white arrow) west within the Jezero candidate landing site ellipse and at the delta toe. Scene is ~150 m wide. Also see Fig. 7d.

Animation S9. An animated time-step sequence of a small barchan dunes (local) southwest of the NE Syrtis candidate landing site ellipse migrating westward (white arrow). Scene is ~275 m wide. Note the slight distortions on the bottom right due to image geometry offsets. Also see Fig. 8e.

Animation S10. An animated time-step sequence of (local) El Dorado ripples showing no evidence of movement other than the difference in local dust deposition in long-baseline images (~5 MY). Location is just southeast of the Columbia Hills candidate landing site ellipse. Scene is ~250 m wide. Also see Fig. 9c.

References:

Atwood-Stone, C., & McEwen, A. S. (2013). Avalanche slope angles in low-gravity environments from active Martian sand dunes. *Geophysical Research Letters*, *40*(12), 2929–2934. https://doi.org/10.1002/grl.50586

Banks, M. E., Geissler, P. E., Bridges, N. T., Russell, P., Silvestro, S., Chojnacki, M., … Delamere, W. A. (2015). Emerging Global Trends in Aeolian Bedform Mobility on Mars (p. Abstract #8036). Presented at the Fourth International Planetary Dunes Workshop: Integrating Models, Remote Sensing, and Field Data, Houston: Lunar and Planetary Institute. Retrieved from http://www.lpi.usra.edu/meetings/dunes2015/pdf/8036.pdf

Bourke, M., Balme, M., Beyer, R., Williams, K., & Zimbelman, J. (2006). A comparison of methods used to estimate the height of sand dunes on Mars. *Geomorphology*, *81*(3–4), 440–452. https://doi.org/10.1016/j.geomorph.2006.04.023

Bridges, N. T., Geissler, P., Silvestro, S., & Banks, M. (2013). Bedform migration on Mars: Current results and future plans. *Aeolian Research*, *9*, 133–151. https://doi.org/10.1016/j.aeolia.2013.02.004

Bridges, N. T., Ayoub, F., Avouac, J.-P., Leprince, S., Lucas, A., & Mattson, S. (2012). Earth-like sand fluxes on Mars. *Nature*, *485*(7398), 339–342. https://doi.org/10.1038/nature11022

Bridges, N. T., Bourke, M. C., Geissler, P. E., Banks, M. E., Colon, C., Diniega, S., … Thomson, B. J. (2011). Planet-wide sand motion on Mars. *Geology*, *40*(1), 31–34. https://doi.org/10.1130/G32373.1

Chojnacki, M., Johnson, J. R., Moersch, J. E., Fenton, L. K., Michaels, T. I., & Bell III, J. F. (2015). Persistent aeolian activity at Endeavour crater, Meridiani Planum,

Mars; new observations from orbit and the surface. *Dynamic Mars*, *251*(0), 275–290. https://doi.org/10.1016/j.icarus.2014.04.044

Chojnacki, M., Burr, D. M., Moersch, J. E., & Michaels, T. I. (2011). Orbital observations of contemporary dune activity in Endeavor crater, Meridiani Planum, Mars. *Journal of Geophysical Research*, *116*. https://doi.org/10.1029/2010JE003675

Chojnacki, M., Urso, A. C., Fenton, L. K., & Michaels, T. I. (2017). Aeolian dune sediment flux heterogeneity in Meridiani Planum, Mars. *Aeolian Research*, *26*, 73–88. https://doi.org/10.1016/j.aeolia.2016.07.004

Golombek, M. P., Grant, J., Kipp, D., Vasavada, A., Kirk, R., Fergason, R., … Watkins, M. (2012). Selection of the Mars Science Laboratory Landing Site. *Space Science Reviews*, *170*(1–4), 641–737. https://doi.org/10.1007/s11214-012-9916-y

Greeley, R., Leach, R. N., Williams, S. H., White, B. R., Pollack, J. B., Krinsley, D. H., & Marshall, J. R. (1982). Rate of wind abrasion on Mars. *Journal of Geophysical Research: Solid Earth*, *87*(B12), 10009–10024. https://doi.org/10.1029/JB087iB12p10009

Hayward, R. K., Fenton, L. K., & Titus, T. N. (2014). Mars Global Digital Dune Database (MGD3): Global dune distribution and wind pattern observations. *Icarus*, *230*(0), 38–46. https://doi.org/10.1016/j.icarus.2013.04.011

Kirk, R. L., Howington-Kraus, E., Redding, B., Galuszka, D., Hare, T. M., Archinal, B. A., … Barrett, J. M. (2003). High-resolution topomapping of candidate MER landing sites with Mars Orbiter Camera narrow-angle images: MER CANDIDATE LANDING SITE TOPOMAPPING. *Journal of Geophysical*

Research: Planets, *108*(E12). https://doi.org/10.1029/2003JE002131

Kirk, R. L., Howington-Kraus, E., Rosiek, M. R., Anderson, J. A., Archinal, B. A., Becker, K. J., … McEwen, A. S. (2008). Ultrahigh resolution topographic mapping of Mars with MRO HiRISE stereo images: Meter-scale slopes of candidate Phoenix landing sites. *Journal of Geophysical Research*, *113*. https://doi.org/10.1029/2007JE003000

Kok, J. F. (2010). Difference in the Wind Speeds Required for Initiation versus Continuation of Sand Transport on Mars: Implications for Dunes and Dust Storms. *Physical Review Letters*, *104*(7). https://doi.org/10.1103/PhysRevLett.104.074502

Mattson, S., Bridges, N. T., Kirk, R. L., Howington-Kraus, E., Mogk, N., & Ojha, L. (2012). Studying Martian Dune Changes with HiRISE DTMs and Orthoimages (p. Abstract #7030). Presented at the Third International Planetary Dunes Workshop: Remote Sensing and Image Analysis of Planetary Dunes, Houston: Lunar and Planetary Institute. Retrieved from http://www.lpi.usra.edu/meetings/dunes2012/pdf/7030.pdf

Ould Ahmedou, D., Ould Mahfoudh, A., Dupont, P., Ould El Moctar, A., Valance, A., & Rasmussen, K. R. (2007). Barchan dune mobility in Mauritania related to dune and interdune sand fluxes. *Journal of Geophysical Research: Earth Surface*, *112*(F2), F02016. https://doi.org/10.1029/2006JF000500

Piqueux, S., Byrne, S., Kieffer, H. H., Titus, T. N., & Hansen, C. J. (2015). Enumeration of Mars years and seasons since the beginning of telescopic exploration. *Dynamic Mars*, *251*, 332–338. https://doi.org/10.1016/j.icarus.2014.12.014

Smith, D. E., Zuber, M. T., Frey, H. V., Garvin, J. B., Head, J. W., Muhleman, D. O., … Sun, X. (2001). Mars Orbiter Laser Altimeter: Experiment summary after the first year of global mapping of Mars. *J. Geophys. Res.*, *106*(E10), 23689–23722. https://doi.org/10.1029/2000JE001364

Sutton, S., Chojnacki, M., Kilgallon, A., & Team, H. (2015). Precision and Accuracy of Simultaneously Collected HiRISE Digital Terrain Models. In *46th Lunar and Planetary Science Conference* (p. Abstract #3010). Houston: Lunar and Planetary Institute. Retrieved from http://www.lpi.usra.edu/meetings/lpsc2015/pdf/3010.pdf